Research Article

Structural, thermomagnetic, and dielectric properties of Mn$_{0.5}$Zn$_{0.5}$Gd$_x$Fe$_{2-x}$O$_4$ (x = 0, 0.025, 0.050, 0.075, and 0.1)

Lakshita PHOR, Vinod KUMAR *

Hydrogen Lab, *Department of Physics*, *DCR University of Science and Technology*, *Murthal-131039*, *Haryana*, *India*

© The Author(s) 2020.

Abstract: In this paper, effect of Gd^{3+} was investigated on structural, magnetic, and dielectric properties of Mn$_{0.5}$Zn$_{0.5}$Gd$_x$Fe$_{2-x}$O$_4$ (x = 0, 0.025, 0.050, 0.075, and 0.1) nanoparticles prepared by facile coprecipitation method. X-ray diffraction (XRD) studies confirmed the single cubic spinel phase for all the samples and showed that lattice parameter (a_{exp}) was found to increase from 8.414 to 8.446 Å with the substitution of Gd^{3+} ions due to their larger ionic radii than the replaced Fe^{3+} ions. Shape and size of developed nanoparticles were studied using transmission electron microscopy (TEM) and found that particle size decreased from 31.06 to 21.12 nm for x = 0–0.1. Magnetic properties showed that maximum magnetization decreased from 39.21 to 23.59 emu/g, and Curie temperature decreased from 192 to 176 ℃ with increase in x from 0 to 0.1 due to weakening of superexchange interaction. Dielectric parameters like dielectric constant (ε' and ε''), dielectric loss (tanδ), AC conductivity (σ_{ac}), and impedance (Z' and Z'') as a function of frequency and composition were analyzed and discussed. It was found that ε', ε'', σ_{ac}, and tanδ values decreased with Gd substitution, which has been explained based on Maxwell–Wagner theory and hopping mechanism of electrons between Fe^{3+} and Fe^{2+} ions at octahedral sites. Nyquist plots for all the developed compositions showed single semi-circular arc which indicate the dominant effect of grain boundaries.

Keywords: spinel ferrite; coprecipitation method; structural property; magnetism; dielectric property

1   Introduction

Mn–Zn ferrites have been considered as one of the most significant soft-magnetic ferrites owing to their higher saturation magnetization, chemical stability, pyromagnetic coefficient ($\Delta M/\Delta T$), superparamagnetic behavior, relatively low Curie temperature (T_C), large permeability up to several MHz, high electrical resistivity, and small power losses. These characteristics facilitate their broad prospect of applications in transformer cores, transducers, magnetic amplifiers, recording heads, and computer chips [1–3]. They are also known to exhibit properties that can be remarkably influenced by temperature and applied magnetic field making them potential contender in ferrofluids, drug delivery, hyperthermia, magnetic separation, and heat transfer [4–7]. Previous reports from literature survey have demonstrated the potential application of Mn–Zn ferrofluid in automatic energy transport devices (AETD)

* Corresponding author.

E-mail: vinod.phy@dcrustm.org

[8,9]. In our recent report, we have investigated the use of Mn–Zn ferrites and their ferrofluids as coolant in self-regulating cooling device due to their favorable magnetic properties [10]. Besides, low conductivity and eddy current losses of Mn–Zn ferrites enable them for telecommunication applications at higher frequencies and energy storage devices. Further, high resistivity can substantially decrease the problems caused by these losses. One proposed way to achieve this can be substitution of suitable dopant, which can increase the grain resistivity by increasing activation energy required for hopping of electrons [11].

Efforts have been made towards understanding the influence of substitution of rare earth (RE) elements on the magnetic and dielectric properties of Mn–Zn ferrites. It is known that larger Gd^{3+} ions exclusively occupy octahedral (B) sites and its substitution for smaller Fe^{3+} ions was found to reduce its magnetization. This can be attributed to the paramagnetic behavior of Gd^{3+} at room temperature [12]. Additionally, RE ions with stable 3+ valence states have been noted to be the best substitution that favors the magnetic properties by reducing the Curie temperature and hence, stimulate the performance of self-cooling devices [10]. Moreover, RE oxides are notable insulators and show high electrical resistivity. Small substitution of RE^{3+} in ferrites can favorably enhance their electromagnetic characteristics by showing good magnetic properties at higher frequencies that can facilitate their application in transformer cores. So, such smart and multifunctional nanomaterials are expected to be promising in many technological applications [13].

In this paper, we have carried out a detailed investigation on the structural, magnetic, and dielectric properties viz. lattice parameter, particle size, maximum magnetization, magnetic moment, Curie temperature, coercivity, retentivity, dielectric constant, dielectric loss, conductivity, etc., of $Mn_{0.5}Zn_{0.5}Fe_2O_4$ nanoparticles as a function of composition (substitution of Gd^{3+} ions), temperature, and frequency.

2　Experimental

2. 1　Characterizations

Structural measurements were performed on Rigaku Ultima-IV in 2θ range of 20°–70° at a rate of 2 (°)/min. Morphology of synthesized samples was elucidated using Thermo scientific (Talos) cryo-transmission electron microscope (TEM). Lake Shore (Model: 7410) vibrating sample magnetometer (VSM) was used to study the magnetic properties at room temperature in the range ±15000 G and temperature dependent measurements at a constant field of 500 G. Dielectric studies were made using nF impedance analyzer in the frequency range of 100 Hz to 1 MHz at room temperature.

2. 2　Synthesis

$Mn_{0.5}Zn_{0.5}Gd_xFe_{2-x}O_4$ (x = 0, 0.025, 0.050, 0.075, and 0.1) were prepared using coprecipitation method. $MnCl_2$, $Zn(NO_3)_2 \cdot 6H_2O$, $Gd(NO_3)_3 \cdot 6H_2O$, and $Fe(NO_3)_3 \cdot 9H_2O$ of analytical grade (Sigma Aldrich) were taken as initial precursors. Stoichiometric ratio of each salt was dissolved in distilled water to obtain homogeneous solution. Then, the solutions were mixed together at constant heating of 60 ℃ with stirring. Oleic acid (surfactant) was added dropwise to avoid agglomeration of nanoparticles and atmospheric oxidation. Later, analytical grade ammonia was added to the solution until the pH was adjusted to 11–12. A constant heating at 85 ℃ was done for one hour for the transformation of hydroxides to ferrites. Then, the sample was washed 3–4 times with ethanol and distilled water which was dried to obtain nanoparticles. The as-prepared nanoparticles were annealed at 500 ℃ in air and used for further characterizations.

3　Results and discussion

3. 1　Structural analysis

X-ray diffraction pattern for nanoparticles under investigation is shown in Fig. 2 which confirmed the single cubic spinel phase for all the samples. Characteristic peaks corresponding to the planes (220), (311), (400), (511), and (440) were detected and matched well with the JCPDS file 74-2401. The crystallite size (D) was calculated about the peak corresponding to plane (311) using the well-known Scherrer's formula [14]:

$$D = \frac{k\lambda}{\beta \cos\theta_{311}} \qquad (1)$$

where the symbols have their usual meanings. Interplanar spacing (d) was used to calculate the lattice parameter (a_{exp}):

$$a_{\text{exp}} = d\sqrt{h^2 + k^2 + l^2} \qquad (2)$$

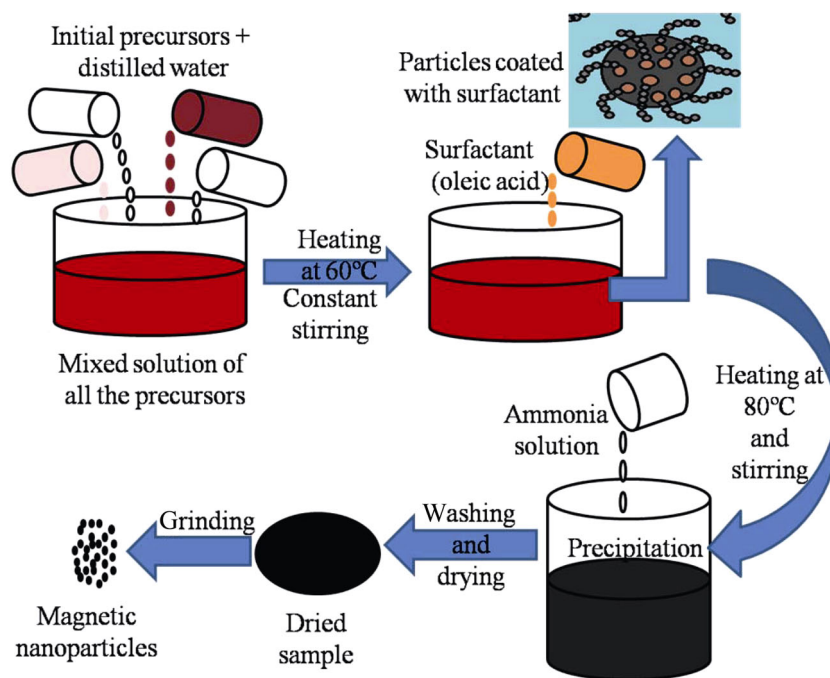It is observed from Table 1 that lattice parameter

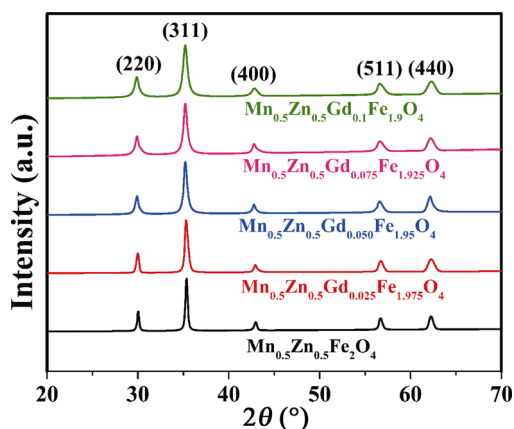**Fig. 1** Schematic diagram of synthesis of developed ferrite nanoparticles.

Fig. 2 XRD patterns for $Mn_{0.5}Zn_{0.5}Gd_xFe_{2-x}O_4$ ($x = 0$, 0.025, 0.05, 0.075, and 0.1) nanoparticles.

(a_{exp}) increases from 8.414 to 8.446 Å with Gd content from 0 to 0.1. This expansion in lattice can be attributed to the incorporation of Gd^{3+} ions (0.938 Å) in the structure with larger ionic radii than replaced Fe^{3+} (0.67 Å) ions at B sites. This causes distortion in lattice and increase in lattice parameter. Similar results of increasing lattice parameter with substitution of larger ions have been reported in literature [10,15,16]. Crystallite size was found to decrease from 25.81 to 13.14 nm with Gd substitution. This can be explained on the basis of lattice expansion that causes lattice strain which in turn produces internal stress, restricting the grain growth [17]. Further, bond energy corresponding to Gd^{3+}–O^{2-} is larger as compared to that of Fe^{3+}–O^{2-}, indicating that energy needed for grain growth and complete crystallization is larger for Gd substituted samples than pristine Mn–Zn ferrite [18,19].

Cation distribution for Gd substituted $Mn_{0.5}Zn_{0.5}Fe_2O_4$ has been proposed and shown in Table 1. In $Mn_{0.5}Zn_{0.5}Gd_xFe_{2-x}O_4$ ferrite, all divalent and trivalent cations occupy 8 A and 16 B sites. In the current case, Zn^{2+} ions exclusively occupy A sites and Mn^{2+} ions occupy B sites. Fe^{3+} ions are distributed over both A and B sublattices and larger Gd^{3+} ions prefer B sites.

Average cationic radii for A and B sublattices (r_A and r_B) are calculated by following relations:

$$r_A = (C^A_{Mn^{2+}})(r_{Mn^{2+}}) + (C^A_{Zn^{2+}})(r_{Zn^{2+}})$$
$$+ (C^A_{Fe^{3+}})(r_{Fe^{3+}}) + (C^A_{Gd^{3+}})(r_{Gd^{3+}}) \qquad (3)$$

Table 1 Cation distribution, variation of lattice parameter, and crystallite size for $Mn_{0.5}Zn_{0.5}Gd_xFe_{2-x}O_4$ ($x = 0$, 0.025, 0.05, 0.075, and 0.1) nanoparticles

x	a_{exp} (Å)	D (nm)	Cation distribution [2]
0	8.414	25.81	$(Zn^{2+}_{0.5}Fe^{3+}_{0.5})^A$ $(Mn^{2+}_{0.5}Fe^{3+}_{1.5})^B$
0.025	8.416	18.28	$(Zn^{2+}_{0.5}Fe^{3+}_{0.5})^A$ $(Mn^{2+}_{0.5}Fe^{3+}_{1.475}Gd^{3+}_{0.025})^B$
0.050	8.440	15.72	$(Zn^{2+}_{0.5}Fe^{3+}_{0.5})^A$ $(Mn^{2+}_{0.5}Fe^{3+}_{1.450}Gd^{3+}_{0.050})^B$
0.075	8.443	14.09	$(Zn^{2+}_{0.5}Fe^{3+}_{0.5})^A$ $(Mn^{2+}_{0.5}Fe^{3+}_{1.425}Gd^{3+}_{0.075})^B$
0.100	8.446	13.14	$(Zn^{2+}_{0.5}Fe^{3+}_{0.5})^A$ $(Mn^{2+}_{0.5}Fe^{3+}_{1.4}Gd^{3+}_{0.1})^B$

$$r_B = \frac{1}{2}[(C^B_{Mn^{2+}})(r_{Mn^{2+}}) + (C^B_{Zn^{2+}})(r_{Zn^{2+}})$$
$$+ (C^B_{Fe^{3+}})(r_{Fe^{3+}}) + (C^B_{Gd^{3+}})(r_{Gd^{3+}})] \qquad (4)$$

where ionic concentration for A and B sublattices are given by C^A and C^B respectively while r_x represents the ionic radius of x ions. Calculated values of average cationic radius at A and B sites are summarized in Table 2. The increase in average cationic radius with Gd content can be a result of expansion of B sites due to substitution of larger Gd^{3+} ions. Theoretically calculated lattice parameter (a_{th}) can be estimated using average cationic and oxygen ion radius (R_O) in Eq. (5) [20]:

$$a_{th} = 8 \frac{r_A + R_O + \sqrt{3}(r_B + R_O)}{3\sqrt{3}} \qquad (5)$$

It may be noted that values of theoretical lattice parameter increase linearly with Gd substitution as shown in Table 2. It is further observed that values of "a_{th}" are greater than that of "a_{exp}" because the former calculations presume a closely packed structure and cations are considered as rigid spheres [21].

The inversion parameter (δ) can be calculated as deviation of oxygen positional parameter (U) from U_{ideal} (0.375) using the following equations [22]:

$$U = \left(\frac{1}{a_{th}\sqrt{3}}\right)(r_A + R_O) + \frac{1}{4} \qquad (6)$$

$$\delta = U - U_{ideal} \qquad (7)$$

The values of U and δ decrease with concentration of Gd^{3+} ions, as shown in Table 2. It is well known that B sites are larger than A sites and hence, it is difficult for cations to occupy A sites. Further, oxygen ions are connected to B sites which causes some expansion or contraction at sublattices due to movement of oxygen ions defined as oxygen positional parameter. The inversion parameter (δ) indicates the trigonal distortion

effect at sublattices as a result of movement of oxygen ions [2].

The bond length for A sites and B sites (R_A and R_B) are calculated by [16]:

$$R_A = a\sqrt{3}\left(\delta + \frac{1}{8}\right) \qquad (8)$$

$$R_B = a\sqrt{3\delta^2 - \frac{\delta}{2} + \frac{1}{16}} \qquad (9)$$

It is seen from Table 3 that bond length at A sites (R_A) decreases and B sites (R_B) increases with Gd substitution. This variation can be understood on the basis of substitution of larger Gd^{3+} ions that causes expansion in B sites and displacement of oxygen ions leading to shrinkage at A sites. The tetrahedral edge length (R_X), the shared octahedral edge length ($R_{X'}$), the unshared octahedral edge length ($R_{X''}$), and X-ray density (ρ_X) are calculated using [3]:

$$R_X = a\sqrt{2}\left(2U - \frac{1}{2}\right) \qquad (10)$$

$$R_{X'} = a\sqrt{2}(1 - 2U) \qquad (11)$$

$$R_{X''} = a\sqrt{4U^2 - 3U + \frac{11}{16}} \qquad (12)$$

$$\rho_X = \frac{Z \times M}{Na^3} \qquad (13)$$

Table 3 summarizes the values of R_X, $R_{X'}$, and $R_{X''}$ for $Mn_{0.5}Zn_{0.5}Gd_xFe_{2-x}O_4$ ($x = 0$–0.1). The variation in the values depends upon a_{exp} and U, which are further influenced by the substitution of Gd content. Variation in density of compounds gives us two useful general remarks: (a) the effectiveness of incorporation of Gd^{3+} ions into $Mn_xZn_{1-x}Fe_2O_4$ and (b) density increases continuously with Gd substitution. The observed

Table 2 Variation of average ionic radius, theoretical lattice parameter, oxygen positional parameter, and inversion parameter for $Mn_{0.5}Zn_{0.5}Gd_xFe_{2-x}O_4$ ($x = 0$, 0.025, 0.05, 0.075, and 0.1) nanoparticles

x	0	0.025	0.050	0.075	0.1
r_A (Å)	0.7050	0.7050	0.7050	0.7050	0.7050
r_B (Å)	0.7075	0.7109	0.7142	0.7176	0.7209
a_{th} (Å)	8.5241	8.5331	8.5420	8.5509	8.5599
U	0.3872	0.3870	0.3869	0.3867	0.3866
δ	0.0122	0.0120	0.0119	0.0117	0.0116

Table 3 Variation of bond length, tetrahedral edge length, the shared octahedral edge length, the unshared octahedral edge length, and X-ray density for $Mn_{0.5}Zn_{0.5}Gd_xFe_{2-x}O_4$ ($x = 0$, 0.025, 0.050, 0.075, and 0.1) nanoparticles

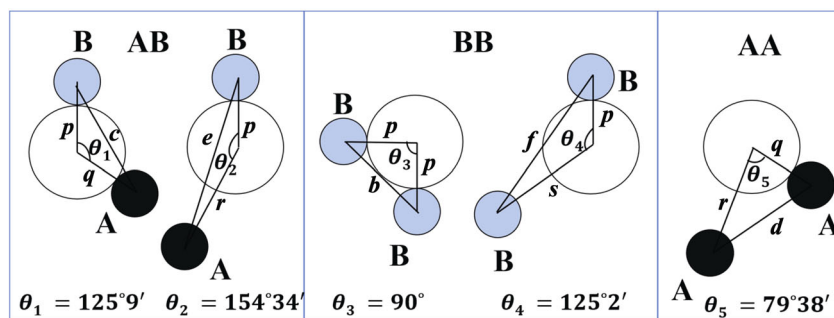| x	0	0.025	0.050	0.075	0.1
R_A (Å)	1.9994	1.9971	2.0013	1.9989	1.9983
R_B (Å)	2.0061	2.0082	2.0147	2.0167	2.0183
R_X (Å)	3.2646	3.2609	3.2677	3.2638	3.2628
$R_{X'}$ (Å)	2.6840	2.6896	2.6996	2.7052	2.7086
$R_{X''}$ (Å)	2.9818	2.9825	2.9909	2.9915	2.9926
ρ_X (g/cm³)	5.2402	5.2911	5.3183	5.3699	5.4235

Fig. 3   Representations of angles and distances between cation–anion and cation–cation at A and B sublattices.

variation in density with Gd substitution is anticipated due to greater atomic weight and density of Gd^{3+} ions (157.25 u and 7.90 g/cm^3) as compared to Fe^{3+} ions (55.845 u and 7.874 g/cm^3).

The cation–anion distances denoted by p, q, r, and s, cation–cation distances by b, c, d, e, and f in as-synthesized samples are estimated using relations (14)–(22) [22].

Cation–anion distances

$$p = a\left(\frac{5}{8} - U\right) \qquad (14)$$

$$q = a\left(U - \frac{1}{4}\right)\sqrt{3} \qquad (15)$$

$$r = a\left(U - \frac{1}{4}\right)\sqrt{11} \qquad (16)$$

$$s = a\left(\frac{1}{3}U + \frac{1}{8}\right)\sqrt{3} \qquad (17)$$

Cation–cation distances

$$b = \left(\frac{a}{4}\right)\sqrt{2} \qquad (18)$$

$$c = \left(\frac{a}{8}\right)\sqrt{11} \qquad (19)$$

$$d = \left(\frac{a}{4}\right)\sqrt{3} \qquad (20)$$

$$e = \left(\frac{3a}{8}\right)\sqrt{3} \qquad (21)$$

$$f = \left(\frac{a}{4}\right)\sqrt{6} \qquad (22)$$

The calculated cation–anion (p, q, r, and s) and cation–cation (b, c, d, e, and f) distances for the synthesized samples are given in Table 4. Values of cation–cation distances for Gd substitution to $Mn_{0.5}Zn_{0.5}Fe_2O_4$ follow the same trend as lattice parameter, whereas variation in

Table 4   Interionic distance for $Mn_{0.5}Zn_{0.5}Gd_xFe_{2-x}O_4$ (x = 0, 0.025, 0.050, 0.075, and 0.10) nanoparticles

x	0	0.025	0.05	0.075	0.1
p (Å)	2.0008	2.0031	2.0097	2.0119	2.0136
q (Å)	1.9994	1.9971	2.0013	1.9989	1.9983
r (Å)	3.8279	3.8236	3.8316	3.8271	3.8258
s (Å)	3.7006	3.7008	3.7108	3.7108	3.7118
b (Å)	2.9747	2.9757	2.9841	2.9849	2.9861
c (Å)	3.4882	3.4893	3.4992	3.5002	3.5016
d (Å)	3.6433	3.6445	3.6548	3.6558	3.6573
e (Å)	5.4650	5.4667	5.4822	5.4837	5.4859
f (Å)	5.1524	5.1540	5.1687	5.1701	5.1722

cation–anion distances depends upon lattice parameter and oxygen positional parameter. Bond angles are calculated using interionic distances using relations [3]:

$$\theta_1 = \cos^{-1}\left(\frac{p^2 + q^2 - c^2}{2pq}\right) \qquad (23)$$

$$\theta_2 = \cos^{-1}\left(\frac{p^2 + r^2 - e^2}{2pr}\right) \qquad (24)$$

$$\theta_3 = \cos^{-1}\left(\frac{2p^2 - b^2}{2p^2}\right) \qquad (25)$$

$$\theta_4 = \cos^{-1}\left(\frac{p^2 + s^2 - f^2}{2ps}\right) \qquad (26)$$

$$\theta_5 = \cos^{-1}\left(\frac{r^2 + q^2 - d^2}{2rq}\right) \qquad (27)$$

The calculated bond angle values with Gd substitution in $Mn_{0.5}Zn_{0.5}Fe_2O_4$ are summarized in Table 5. It is known that increase in bond angle indicates strengthening of respective cation–anion/cation–cation interactions whereas decreasing values suggest weakening of corresponding interactions. It is noted that the angles θ_1, θ_2, and θ_5 increased while θ_3 and θ_4 decreased with

Table 5 Variation of bond angle for $Mn_{0.5}Zn_{0.5}Gd_xFe_{2-x}O_4$ ($x = 0$, 0.025, 0.050, 0.075, and 0.1) nanoparticle

x	0	0.025	0.05	0.075	0.1
θ_1 (degree)	121.387	121.449	121.478	121.544	121.57
θ_2 (degree)	137.038	137.273	137.388	137.628	137.745
θ_3 (degree)	96.0416	95.9344	95.8768	95.7726	95.7167
θ_4 (degree)	126.701	126.678	126.665	126.643	126.63
θ_5 (degree)	69.435	69.5897	69.7901	69.8237	69.9012

Gd content in Mn–Zn ferrite signifying strong A–B and A–A, and weak B–B interactions [16].

3. 2   Transmission electron microscopy (TEM) analysis

TEM images of $Mn_{0.5}Zn_{0.5}Gd_xFe_{2-x}O_4$ ($x = 0$, 0.05, and 0.1) respectively are shown in Fig. 4 to probe their morphology and average particle size. It is found that average particle size decreases as 31.06, 25.95, and 21.12 nm for Gd content $x = 0$, 0.05, and 0.1 respectively as shown in histograms of Fig. 4. Internal stress produced as a result of lattice distortion can be accounted for the hinderance in grain growth [17]. The particle size estimated from TEM is in well agreement with the crystallite size determined from XRD. Some agglomeration is also observed which can be attributed to magnetic interactions among nanoparticles.

3. 3   Magnetic measurements

Figure 5 shows the magnetization as a function of magnetic field for pristine and gadolinium substituted $Mn_{0.5}Zn_{0.5}Gd_xFe_{2-x}O_4$ from $x = 0$ to 0.1 at 300 K. It is noted that magnetization does not saturate even at higher field of 15,000 G which can be attributed to the superparamagnetic behavior of nanoparticles and non-uniform distribution of particle size [3]. The values of maximum magnetization (M_{max}), coercivity (H_C), retentivity (M_R), squareness (S), anisotropy constant (K), magnetic moment (μ_B), and Curie temperature (T_C) have been summarized in Table 6. Magnetic properties viz. anisotropy constant (K), magnetic moment (η_B), and squareness (S) have been calculated using following equations [3,23]:

$$K = \frac{H_C M_{max}}{0.96} \tag{28}$$

$$S = \frac{M_R}{M_{max}} \tag{29}$$

$$\eta_B = \frac{MW \times M_{max}}{5585} \tag{30}$$

where 5585 is the magnetic factor and MW is the molecular weight.

It is noticed that maximum magnetization decreases continuously from 39.21 to 23.59 emu/g (at 15,000 G) on increasing the Gd content from $x = 0$ to $x = 0.1$ in $Mn_{0.5}Zn_{0.5}Gd_xFe_{2-x}O_4$. The variation in M_{max} can be understood on the basis of cation distribution over A and B sites. The magnetic order in spinel ferrites is
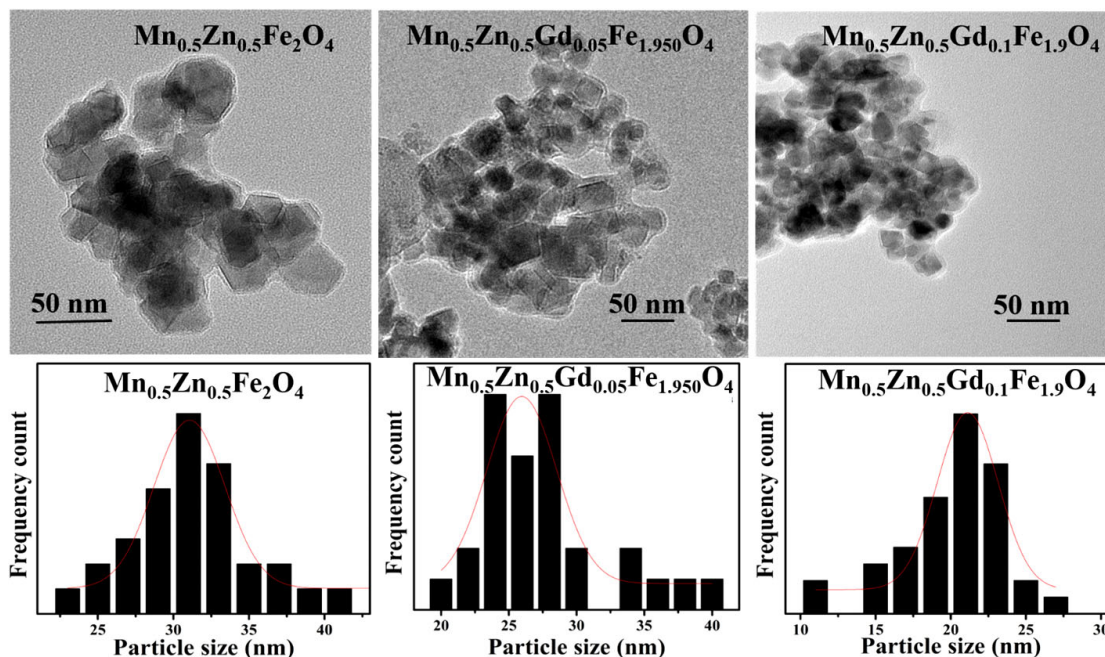

Fig. 4   TEM images of $Mn_{0.5}Zn_{0.5}Gd_xFe_{2-x}O_4$ ($x = 0$, 0.05, and 0.1) nanoparticles along with their histograms.

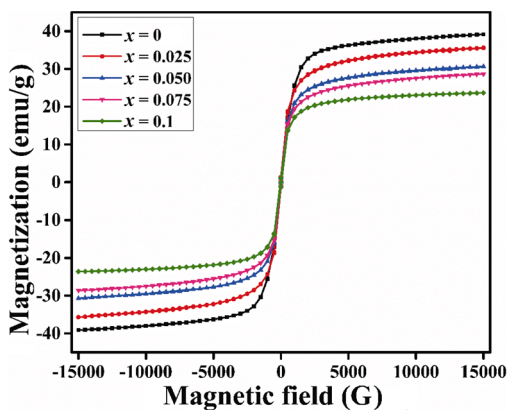**Fig. 5** Variation of magnetization with magnetic field at room temperature for $Mn_{0.5}Zn_{0.5}Gd_xFe_{2-x}O_4$ (x = 0, 0.025, 0.050, 0.075, and 0.1) nanoparticles.

Table 6 Values of M_{max}, H_C, M_R, K, S, η_B, and T_C for $Mn_{0.5}Zn_{0.5}Gd_xFe_{2-x}O_4$ (x = 0, 0.025, 0.050, 0.075, and 0.1) nanoparticles

x	M_{max} (emu/g)	H_C (G)	M_R (emu/g)	K (erg/Oe)	S	η_B (μ_B)	T_C (℃)
0	39.21	34.55	1.49	1411.15	0.038	1.66	192
0.025	35.66	34.54	1.35	1283.02	0.037	1.52	—
0.05	30.69	31.53	0.88	1007.97	0.029	1.32	—
0.075	28.56	36.26	1.38	1078.74	0.048	1.25	—
0.1	23.59	34.58	0.94	849.73	0.039	1.04	176

primarily due to superexchange (A–B) interactions developed between tetrahedral and octahedral sites through oxygen ions [24]. Hence, the net magnetization between oppositely magnetized A and B sublattices is given by $|M_S| = |M_B - M_A|$ where M_A and M_B denote the net magnetic moment at A and B sites respectively [25]. Further, rare earth metals are known to be strongly paramagnetic in nature at room temperature [12]. Due to the larger ionic radius of Gd^{3+} ions (0.938 Å), they occupy B sites and replace smaller Fe^{3+} ions (0.67 Å). Hence, as the substitution of non-magnetic Gd^{3+} ions is increased, the total magnetic moment at B sites (M_B) reduces, consequently reducing the maximum magnetization. Moreover, the decrease in maximum magnetization with Gd content may also be attributed to the decreasing stronger Fe^{3+}–Fe^{3+} (B–B) interactions. Although, Gd^{3+}–Fe^{3+} and Gd^{3+}–Gd^{3+} interactions are present but are weak [25]. Particle size is also known to play an important role in influencing the magnetic properties of ferrites. It has been observed that particle size of nanoparticles decreases with the substitution of Gd and thus, surface to volume ratio increases and canted spins present on the surface reduces the net magnetization of the material. Magnetic moment *(η_B)* values for all the samples are given in Table 6 and are observed to decrease from 1.66 to 1.04 μ_B due to substitution of non-magnetic Gd^{3+} ions for Fe^{3+} ions at B sites. Small values of coercivity and retentivity indicate the superparamagnetic behavior of the synthesized samples. Further, coercivity is known to be influenced by anisotropic field in a way that decreasing anisotropy constant reduces coercivity [26,27]. Also, the existence of Fe^{2+} ions in ferrites accounts for the presence of magnetic anisotropy which decreases upon substitution

of Gd^{3+} ions for Fe^{3+} ions. This in turn, decreases anisotropy constant and so the coercivity. The variation in magnetic properties can be attributed to the contribution of cation distribution over sublattices, random canting of surface spins, dead layer formed on the surface, adsorbed water present in the samples, etc. Squareness (S) is a dimensionless quantity derived from hysteresis loop which indicates the presence or absence of inter-grain interaction. It was reported by Stoner and Wahlfarth [28] that S = 0.5 for non-interacting randomly oriented particles whereas $S < 0.5$ for particles interacting through magnetostatic interaction. Squareness in this case is less than 0.5 for all the compositions indicating magnetostatic interaction between particles.

Variation in magnetization as a function of temperature at a constant field of 500 G is shown in Fig. 6 and the temperature where magnetization becomes zero is noted as Curie temperature (T_C). At Curie temperature, the magnetic energy is overpowered by thermal energy that causes disorder in the system and transition from ferromagnetic to paramagnetic substance takes place [17]. Values of Curie temperature were noted as 192 and 176 ℃ for x = 0 and 0.1 compositions of Gd

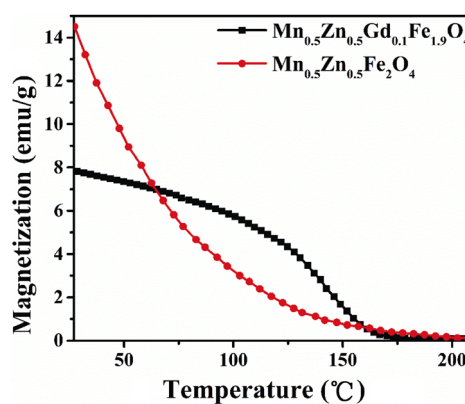**Fig. 6** Magnetization versus temperature at 500 G for $Mn_{0.5}Zn_{0.5}Gd_xFe_{2-x}O_4$ (x = 0 and 0.1) nanoparticles.

respectively. It is well known that B–B and A–B exchange interactions play an important role in influencing the magnetic properties. The decrease in Curie temperature of Gd^{3+} substituted materials can be attributed to the weakening of these interactions due to paramagnetic behavior of Gd^{3+} ions. With the gradual replacement of Fe^{3+} ions by Gd^{3+} ions, number of magnetic Fe^{3+} ions at B sites decreases and consequently, weakens the A–B and B–B interactions. Hence, the temperature (thermal energy) needed to counterbalance the spin order decreases, so decreasing the Curie temperature [29,30]. Owing to the larger bond energy of Gd^{3+}–O^{2-} as compared to that of Fe^{3+}–O^{2-}, Gd^{3+} substituted ferrites have higher thermal stability relative to pure $Mn_{0.5}Zn_{0.5}Fe_2O_4$ ferrite [18,19]. As a result of this enhanced thermal stability of Gd substituted Mn–Zn ferrite, it is observed from Fig. 6 that above 100 ℃, magnetic energy is overpowered by thermal energy causing disorder in the system and hence, different trends are observed in both the M–T curves. In the $Mn_{0.5}Zn_{0.5}Gd_{0.1}Fe_{1.9}O_4$ sample shown in Fig. 6, we get low pyromagnetic coefficient at lower temperatures, which is good for applications in transformer core owning to their higher thermal stability. Also, higher pyromagnetic coefficient near the Curie temperature range makes these materials to have applications in ferrofluid based self-cooling devices [10].

3.4 Dielectric analysis

3.4.1 Dielectric constant study

Dielectric constant (ε) in an applied AC field can be represented in a complex form as $\varepsilon^* = \varepsilon' + i\varepsilon''$ where the real part is relative dielectric constant or real permittivity and corresponds to the amount of polarization energy stored in a dielectric material while the imaginary part refers to the energy loss that provides dissipated energy. Real (ε') and imaginary (ε'') parts of dielectric constant can be evaluated using following relations:

$$\varepsilon' = \frac{C_p d}{\varepsilon_0 A} \qquad (31)$$

$$\varepsilon'' = \varepsilon' \tan\delta \qquad (32)$$

where C_P is the parallel capacitance, ε_0 is the permittivity of free space, d and A are thickness and cross-sectional area of the pallet respectively. The ratio ($\varepsilon''/\varepsilon'$) is dissipation factor or $\tan\delta$, where δ is the phase difference between applied field and induced current.

Figures 7 and 8 show the variation of ε' and ε'' with frequency in the range 100 Hz–1 MHz at room temperature. It is seen that both ε' and ε'' decrease swiftly with frequency initially and gradually become constant for higher values of frequencies which is a typical dielectric behavior [31–33]. This behavior can be understood on the basis of Maxwell–Wagner model [33] and Koops theory [34], which suggested the inhomogeneous structure of dielectric material. Generally, ferrites are made up of conducting grains which are separated by non-conducting grain boundaries. At lower frequencies, grain boundaries are more effective than grains, whereas grains predominate grain boundaries at higher frequencies. Dielectric constant is influenced by four types of polarizations: (1) space charge polarization; (2) dipolar polarization; (3) ionic polarization; and
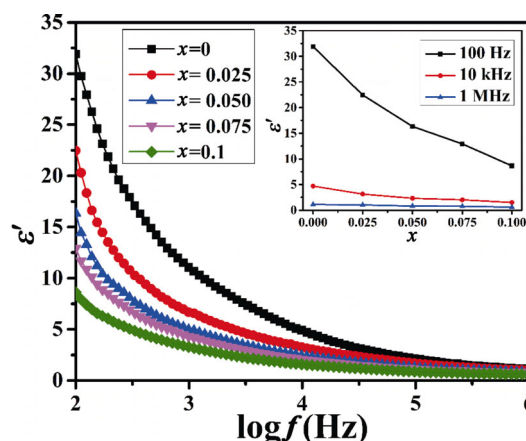
Fig. 7 Variation of real part of dielectric constant of $Mn_{0.5}Zn_{0.5}Gd_xFe_{2-x}O_4$ (x = 0, 0.025, 0.050, 0.075, and 0.10) with frequency.
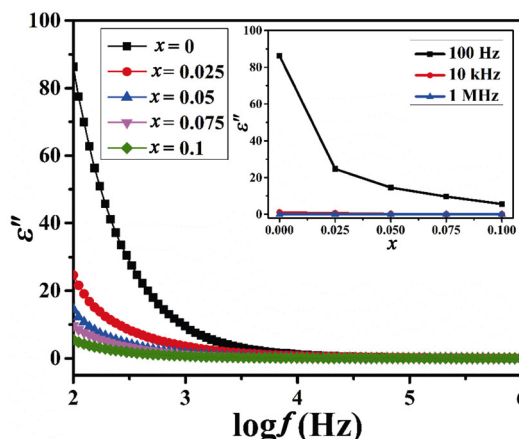
Fig. 8 Variation of imaginary part of dielectric constant of $Mn_{0.5}Zn_{0.5}Gd_xFe_{2-x}O_4$ (x = 0, 0.025, 0.050, 0.075, and 0.10) with frequency.

(4) electronic polarization. At lower frequencies, the contribution of temperature dependent space charge and dipolar polarization becomes dominant while ionic and electronic polarizations play an effective role at higher frequencies [3,35]. High dielectric constant values at low frequencies can be attributed to the space charge polarization effects which are due to hopping of charge carriers between the ions of same element present in at least two valence states [36]. So, when the field is applied, hopping of electrons between Fe^{3+} and Fe^{2+} ions results in electrons piling up at grain boundaries and causes space charge polarization. This contributes to higher values of dielectric constant at lower frequencies. Further, when the frequency of applied field is increased, the electron exchange between Fe^{3+} and Fe^{2+} ions cannot follow the rapidly changing field [24]. The electron will hardly transfer before the alternating field reverses and as a result probability of electrons reaching the grain boundary becomes very less. Consequently, the contribution of space charge polarization decreases causing the dielectric constant value to decrease [37]. Further, it is observed that dielectric constant decreases with increasing x in $Mn_{0.5}Zn_{0.5}Gd_xFe_{2-x}O_4$. This can be explained in view of the fact that Gd^{3+} ions prefer to occupy B sites due to their larger ionic radii and hence diluting Fe^{3+} ions from B sites. This limits the exchange of electrons between Fe^{3+} and Fe^{2+} ($Fe^{3+} + e^- \rightarrow Fe^{2+}$) by violating Verway's hopping process.

3.4.2 Dielectric loss study

Variation of loss factor ($\tan\delta$) as a function of frequency is shown in Fig. 9. It is observed that $\tan\delta$ values decrease sharply for lower frequencies and then become constant for higher values. Hudson [38] showed that variation in dielectric loss in the case of ferrites is well reflected in the conductivity such that materials with high conductivity exhibit higher dielectric loss. Effective role of grain boundaries at lower frequencies can be accounted for high dielectric loss at lower frequency region. Since, more energy is required for hopping of electrons between Fe^{3+} and Fe^{2+} ions at lower frequencies due to highly resistive grain boundaries that lead to maximum loss of energy. However, at higher frequencies even small quantity of energy is enough for exchange of electrons that corresponds to minimum loss of energy [39,40]. Further, it is observed that values of $\tan\delta$ are compositional dependent such that with increase in substitution of Gd^{3+} ions, dielectric
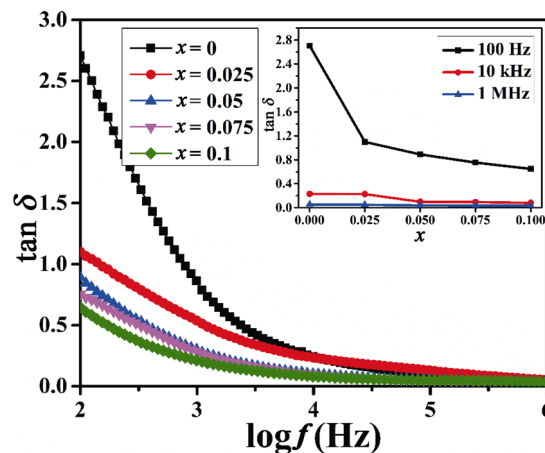
Fig. 9 Variation of dielectric loss of $Mn_{0.5}Zn_{0.5}Gd_xFe_{2-x}O_4$ ($x = 0$, 0.025, 0.050, 0.075, and 0.10) with frequency.

loss decreases. This can be understood as a result of reduced hopping of charge carriers between ferric and ferrous ions as Gd^{3+} ions substitute Fe^{3+} ions at B sites.

3.4.3 AC conductivity study

The plot of AC conductivity with frequency (100 Hz–1 MHz) for all the samples is shown in Fig. 10 to study the transport mechanism. AC conductivity has been evaluated using following relation:

$$\sigma_{ac} = 2\pi f \varepsilon' \varepsilon_0 \tan\delta \tag{33}$$

where f is the frequency in Hz. It is noted that σ is almost constant at low frequencies and then shows sharp increment at high frequencies. This pattern can be justified in view of Maxwell–Wagner model; the conduction process in low frequency region is mainly due to poorly conducting grain boundaries whereas conducting grains play an effective role at higher
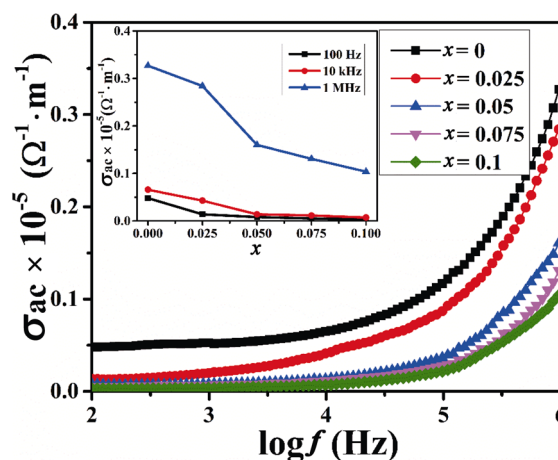
Fig. 10 Variation of AC conductivity of $Mn_{0.5}Zn_{0.5}Gd_xFe_{2-x}O_4$ ($x = 0$, 0.025, 0.050, 0.075, and 0.10) with frequency.

frequencies as discussed above. Therefore, the constant low conductivity values at low frequencies are attributed to the highly resistive grain boundaries that lead to slower exchange of electrons. However, conducting grains accelerate the hopping of electrons at high frequencies hence increasing the conductivity [41]. Furthermore, increase in AC conductivity is related to increase in rate of exchange of charge carriers and not the number of charge carriers. Since the electrons follow the applied field, so, as the frequency of applied field increases, exchange of charge carriers increases [42]. This results in gradual increase of AC conductivity with applied frequency. Effect of composition on σ_{ac} shows that by increasing Gd^{3+} ions concentration, AC conductivity is found to decrease due to restricted hopping of electrons between Fe^{2+} and Fe^{3+} ions as Gd ions substitute Fe^{3+} ions at B sites and do not participate in conduction process. Further, it has been observed that grain size deceases with Gd substitution which increases the contribution of grain boundaries hence decreasing the conductivity.

3.4.4 Impedance analysis

Impedance spectroscopy is considered as convenient and useful technique to explore the electrical characteristics of materials whose properties are influenced by composition, dopant, dopant distribution, and ceramic texture. Permittivity (ε^{*}), impedance (Z^{*}), modulus (M^{*}) can be related to dielectric loss (tanδ) using following equation:

$$\tan \delta = \frac{\varepsilon''}{\varepsilon'} = \frac{Z'}{Z''} = \frac{M''}{M'} \tag{34}$$

Variation of real (Z') and imaginary (Z'') impedance as a function of frequency in the range 100 Hz–1 MHz for all the samples is shown in Figs. 11 and 12. It is observed that Z' decreases with frequency and eventually merges and shows frequency independent behavior at higher frequencies indicating relaxation effects. The observed trend in Z' versus frequency plot is attributed to the reduced space charge polarization with increasing frequency. Moreover, increase of AC conductivity supports the decreasing pattern of impedance with frequency. Analysis of Fig. 12 showed that broad Debye peak appearing for each sample seems to shift towards the lower frequency as the Gd substitution increases. Here, each Debye peak corresponds to the resonance frequency, which refers to probability of electrons exchange at B sites [36,43]. Further, with increase in Gd^{3+} ions substitution for Fe^{3+}
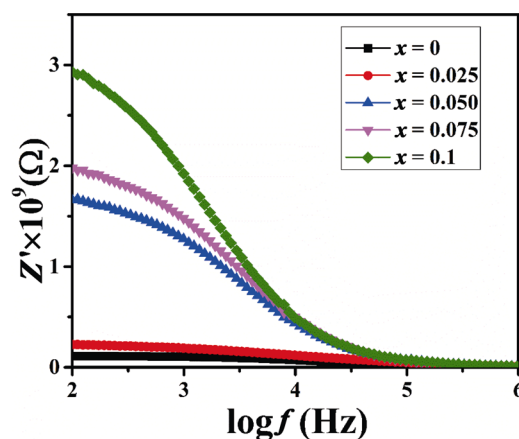

Fig. 11 Variation of real part of impedance of $Mn_{0.5}Zn_{0.5}Gd_xFe_{2-x}O_4$ (x = 0, 0.025, 0.050, 0.075, and 0.10) with frequency.
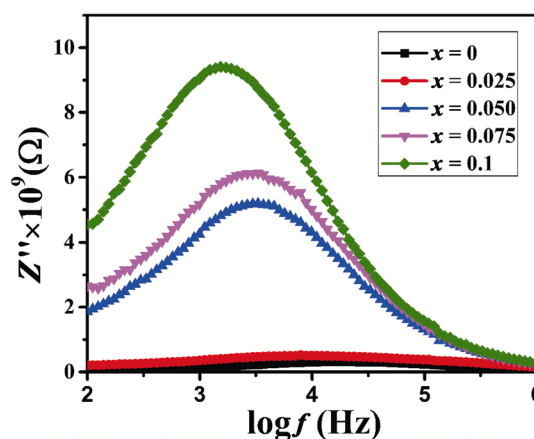

Fig. 12 Variation of imaginary part of impedance of $Mn_{0.5}Zn_{0.5}Gd_xFe_{2-x}O_4$ (x = 0, 0.025, 0.050, 0.075, and 0.10) with frequency.

ions at B sites, probability of hopping of electrons decreases and as a result, resonance frequency shifts towards lower frequencies. This behavior is consistent with other studied dielectric parameters like dielectric constant, loss and conductivity.

The Nyquist plot obtained by plotting Z'' vs. Z' allows us to study the role of grains and grain boundaries in the conduction mechanism. Nyquist plot is based on double layer model and generally shows two semicircular arcs. The semicircular arc obtained at lower frequencies is due to contribution of resistive grain boundaries while grain conduction accounts for the one in high frequency region. Figure 13 shows the Nyquist plot for all the developed compositions of $Mn_{0.5}Zn_{0.5}Gd_xFe_{2-x}O_4$ ferrites. In current case, single semi-circular arc can be observed suggesting the effective role of grain boundaries in conduction [3,36].
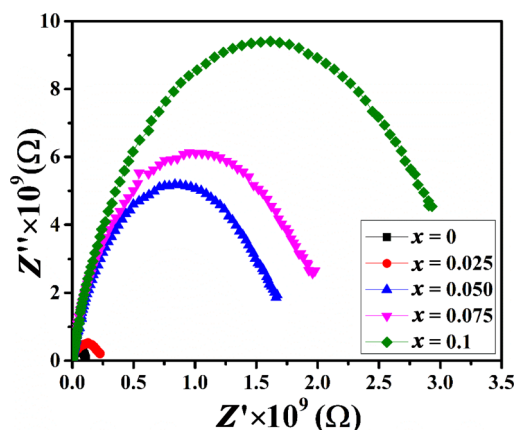
Fig. 13 Nyquist plots for $Mn_{0.5}Zn_{0.5}Gd_xFe_{2-x}O_4$ ($x = 0$, 0.025, 0.050, 0.075, and 0.10).

On further analysis of plot, it is noted that with increase in Gd substitution, the diameter of semicircular arc increases indicating reduced conductivity and increased relaxation time. It can be seen from Nyquist plot that semicircular arc merges and terminates at Z' axis at high frequency region, which represents the bulk resistance.

4   Conclusions

In this paper, Gd substituted $Mn_{0.5}Zn_{0.5}Fe_2O_4$ spinel ferrites were synthesized by simple and cost-effective coprecipitation method. Schematic structural studies by XRD confirmed the single cubic spinel phase for all the samples and various structural parameters like crystallite size, lattice parameter, average ionic radius, bond length, and bond angle were calculated and discussed. Lattice parameter (a_{exp}) was noted to increase with Gd content in $Mn_{0.5}Zn_{0.5}Fe_2O_4$ due to the incorporation of larger Gd^{3+} ions than replaced smaller Fe^{3+} ions at B sites. Morphological investigations using TEM showed that particle size decreased from 31.06 to 21.12 nm with $x = 0$–0.1 as a result of internal stress which restricts the grain growth. Magnetic measurements revealed that with Gd^{3+} concentration from 0 to 0.1, maximum magnetization decreased from 39.21 to 23.59 emu/g and T_C from 192 to 176 ℃. This can be attributed to the paramagnetic nature of Gd, which reduces the magnetic moment at B sites and weakens A–B and B–B interactions. In addition, negligibly small values of coercivity and retentivity indicated the superparamagnetic behavior of developed nanoparticles. Dielectric studies carried out in the frequency range 100 Hz–1 MHz showed that dielectric constant, dielectric loss, and AC conductivity decreased with the

Gd substitution which has been explained based on Maxwell–Wagner theory and hopping mechanism of electrons between Fe^{3+} and Fe^{2+} ions at B sites. The developed nanoparticles with superior magnetic properties such as high saturation magnetization, low T_C, high pyromagnetic coefficient, and superparamagnetism facilitate their application in automatic energy transfer devices. Besides, reduced conductivity and hence, eddy current loss can be considered as an efficient material for high frequency applications.

References

[1]   Deepty M, Srinivas C, Vijaya Babu K, *et al*. Structural and electron spin resonance spectroscopic studies of $Mn_xZn_{1-x}Fe_2O_4$ ($x = 0.5, 0.6, 0.7$) nanoferrites synthesized by sol-gel auto combustion method. *J Magn Magn Mater* 2018, **466**: 60–68.

[2]   Thakur P, Sharma R, Kumar M, *et al*. Superparamagnetic La doped Mn–Zn nano ferrites: Dependence on dopant content and crystallite size. *Mater Res Express* 2016, **3**: 075001.

[3]   Phor L, Kumar V. Structural, magnetic and dielectric properties of lanthanum substituted $Mn_{0.5}Zn_{0.5}Fe_2O_4$. *Ceram Int* 2019, **45**: 22972–22980.

[4]   Brusentsova TN, Kuznetsov VD. Synthesis and investigation of magnetic properties of substituted ferrite nanoparticles of spinel system $Mn_{1-x}Zn_x[Fe_{2-y}L_y]O_4$. *J Magn Magn Mater* 2007, **311**: 22–25.

[5]   Li ML, Fang HY, Li HL, *et al*. Synthesis and characterization of MnZn ferrite nanoparticles with improved saturation magnetization. *J Supercond Nov Magn* 2017, **30**: 2275–2281.

[6]   Yoo D, Lee JH, Shin TH, *et al*. Theranostic magnetic nanoparticles. *Acc Chem Res* 2011, **44**: 863–874.

[7]   Pankhurst QA, Connolly J, Jones SK, *et al*. Applications of magnetic nanoparticles in biomedicine. *J Phys D: Appl Phys* 2003, **36**: R167–R181.

[8]   Lian WL, Xuan YM, Li Q. Design method of automatic energy transport devices based on the thermomagnetic effect of magnetic fluids. *Int J Heat Mass Tran* 2009, **52**: 5451–5458.

[9]   Li Q, Lian WL, Sun H, *et al*. Investigation on operational characteristics of a miniature automatic cooling device. *Int J Heat Mass Tran* 2008, **51**: 5033–5039.

[10] Phor L, Kumar V. Self-cooling device based on thermomagnetic effect of $Mn_xZn_{1-x}Fe_2O_4$ ($x = 0.3, 0.4, 0.5, 0.6, 0.7$)/ferrofluid. *J Mater Sci: Mater Electron* 2019, **30**: 9322–9333.

[11] Shokrollahi H, Janghorban K. Influence of additives on the magnetic properties, microstructure and densification of Mn–Zn soft ferrites. *Mat Sci Eng B* 2007, **141**: 91–107.

[12] Cullity BD. *Introduction to Magnetic Materials*. Addison-Wesley Publishing Co. Inc., 1972: 179.

[13] Rezlescu N, Rezlescu E, Popa P, *et al*. Effects of rare-earth

oxides on physical properties of Li–Zn ferrite. *J Alloys Compd* 1998, **275–277**: 657–659.

[14] Cullity BD. *Elements of X-ray Diffraction*. Reading, MA, USA: Addison-Wesley, 1978.

[15] Chahal S, Rani N, Kumar A, *et al*. UV-irradiated photocatalytic performance of yttrium doped ceria for hazardous Rose Bengal dye. *Appl Surf Sci* 2019, **493**: 87–93.

[16] Mohammed KA, Al-Rawas AD, Gismelseed AM, *et al*. Infrared and structural studies of $Mg_{1-x}Zn_xFe_2O_4$ ferrites. *Physica B* 2012, **407**: 795–804.

[17] Islam R, Hakim MA, Rahman MO, *et al*. Study of the structural, magnetic and electrical properties of Gd-substituted Mn–Zn mixed ferrites. *J Alloys Compd* 2013, **559**: 174–180.

[18] Jiang J, Yang YM. Effect of Gd substitution on structural and magnetic properties of Zn–Cu–Cr ferrites prepared by novel rheological technique. *Mater Sci Technol* 2009, **25**: 415–418.

[19] Meng YY, Liu ZW, Dai HC, *et al*. Structure and magnetic properties of $Mn(Zn)Fe_{2-x}RE_xO_4$ ferrite nano-powders synthesized by co-precipitation and refluxing method. *Powder Technol* 2012, **229**: 270–275.

[20] Mazen SA, Abdallah MH, Sabrah BA, *et al*. The effect of titanium on some physical properties of $CuFe_2O_4$. *Phys Stat Sol (a)* 1992, **134**: 263–271.

[21] Groń T. Influence of vacancies and mixed valence on the transport processes in solid solutions with the spinel structure. *Philos Mag B* 1994, **70**: 121–132.

[22] Zaki HM, Al-Heniti SH, Elmosalami TA. Structural, magnetic and dielectric studies of copper substituted nano-crystalline spinel magnesium zinc ferrite. *J Alloys Compd* 2015, **633**: 104–114.

[23] Kumari N, Kumar V, Khasa S, *et al*. Chemical synthesis and magnetic investigations on Cr^{3+} substituted Zn-ferrite superparamagnetic nano-particles. *Ceram Int* 2015, **41**: 1907–1911.

[24] Thorat LM, Patil JY, Nadargi DY, *et al*. Co^{2+} substituted Mg–Cu–Zn ferrite: Evaluation of structural, magnetic, and electromagnetic properties. *J Adv Ceram* 2018, **7**: 207–217.

[25] Amiri S, Shokrollahi H. Magnetic and structural properties of RE doped Co-ferrite (RE = Nd, Eu, and Gd) nano-particles synthesized by co-precipitation. *J Magn Magn Mater* 2013, **345**: 18–23.

[26] Sattar AA, Samy AM, El-Ezza RS, *et al*. Effect of rare earth substitution on magnetic and electrical properties of Mn–Zn ferrites. *Phys Stat Sol (a)* 2002, **193**: 86–93.

[27] Gorter EW. Saturation magnetization and crystal chemistry of ferrimagnetic oxides. I. II. Theory of ferrimagnetism. *Philips Res Rep* 1954, **9**: 295.

[28] Stoner EC, Wohlfarth EP. A mechanism of magnetic hysteresis in heterogeneous alloys. *Philos T Roy Soc A* 1948, **240**: 599–642.

[29] Arcos D, Valenzuela R, Vázquez M, *et al*. Chemical homogeneity of nanocrystalline Zn–Mn spinel ferrites obtained by high-energy ball milling. *J Solid State Chem* 1998, **141**: 10–16.

[30] Cullity BD, Graham CD. *Introduction to Magnetic Materials*. Hoboken, NJ, USA: John Wiley & Sons, Inc., 2008.

[31] Xing QK, Peng ZJ, Wang CB, *et al*. Doping effect of Y^{3+} ions on the microstructural and electromagnetic properties of Mn–Zn ferrites. *Physica B* 2012, **407**: 388–392.

[32] Rana A, Thakur OP, Kumar V. Effect of Gd^{3+} substitution on dielectric properties of nano cobalt ferrite. *Mater Lett* 2011, **65**: 3191–3192.

[33] Wagner KW. Zur Theorie der unvollkommenen Dielektrika. *Ann Phys* 1913, **345**: 817–855.

[34] Koops CG. On the dispersion of resistivity and dielectric constant of some semiconductors at audiofrequencies. *Phys Rev* 1951, **83**: 121.

[35] Pradhan DK, Kumari S, Puli VS, *et al*. Correlation of dielectric, electrical and magnetic properties near the magnetic phase transition temperature of cobalt zinc ferrite. *Phys Chem Chem Phys* 2017, **19**: 210–218.

[36] Rezlescu N, Rezlescu E. Dielectric properties of copper containing ferrites. *Phys Stat Sol (a)* 1974, **23**: 575–582.

[37] Kumari N, Kumar V, Singh SK. Effect of Cr^{3+} substitution on properties of nano-$ZnFe_2O_4$. *J Alloys Compd* 2015, **622**: 628–634.

[38] Ali A, Grössinger R, Imran M, *et al*. Magnetic and high-frequency dielectric parameters of divalent ion-substituted W-type hexagonal ferrites. *J Electron Mater* **46**: 903–910.

[39] Bhandare MR, Jamadar HV, Pathan AT, *et al*. Dielectric properties of Cu substituted $Ni_{0.5-x}Zn_{0.3}Mg_{0.2}Fe_2O_4$ ferrites. *J Alloys Compd* 2011, **509**: L113–L118.

[40] Jnaneshwara DM, Avadhani DN, Daruka Prasad B, *et al*. Effect of zinc substitution on the nanocobalt ferrite powders for nanoelectronic devices. *J Alloys Compd* 2014, **587**: 50–58.

[41] Kumari N, Kumar V, Singh SK. Synthesis, structural and dielectric properties of Cr^{3+} substituted Fe_3O_4 nano-particles. *Ceram Int* 2014, **40**: 12199–12205.

[42] Chavan P, Naik LR, Belavi PB, *et al*. Studies on electrical and magnetic properties of Mg-substituted nickel ferrites. *J Electron Mater* 2017, **46**: 188–198.

[43] Bindu K, Ajith KM, Nagaraja HS. Electrical, dielectric and magnetic properties of Sn-doped hematite (α-$Sn_xFe_{2-x}O_3$) nanoplates synthesized by microwave-assisted method. *J Alloys Compd* 2018, **735**: 847–854.